

Satellite systems and interactions

I. Matthew Watson, Anupma Prakash

2.1 INTRODUCTION AND BACKGROUND

Remote sensing can be defined as “study of a target (object or phenomenon) where no physical contact with that target is made.” Instead of deriving information from direct contact, the effects of the target on the sensor, typically through some change in the information perceived, are used to derive information about the object or phenomenon. Touching the electric ring of an oven and discovering it is hot is an example of direct sampling. Observing that the ring is glowing red and deducing it is hot is the remote-sensing analog. Thus satellite-based investigation, by definition, relies on remote-sensing techniques.

Remote-sensing techniques are of considerable utility to volcanologists (e.g., Mouginiis-Mark *et al.*, 2000). By their very nature they provide observers with the opportunity to study from a distance what can be an extremely hazardous natural phenomenon. Also, the potential scale of volcanic activity lends itself to the synoptic perspective afforded by satellite-based instruments. Volcanoes may also be geographically remote, such as the Aleutians and Kuriles, or in areas of political unrest, such as in Central and Eastern Africa. Satellite remote sensing negates these problems and provides consistency and continuity of data over large areas of the Earth on a regular basis.

Volcano remote sensing is typically, though not exclusively, the study of the effects of volcanic processes on electromagnetic (EM) radiation (defined and detailed in Section 2.2) which is either gener-

ated naturally (e.g., the Sun, thermal radiation from lava flows) or artificially (e.g., laser, radar). This chapter focuses on the theory of generation, propagation, and interaction of EM radiation with volcanoes and their associated products within a wavelength range from $0.3\ \mu\text{m}$ ($3 \times 10^{-7}\ \text{m}$, ultraviolet light) through $1\ \text{m}$ (microwaves). The aim of this chapter is to ground the reader in the necessary background of the transfer of radiation and its applied uses in remote sensing of volcanoes.

2.2 THE ELECTROMAGNETIC SPECTRUM

2.2.1 Overview, nomenclature, and mathematical framework (see Table 2.1)

Electromagnetic (EM) radiation is produced by all objects with a temperature above absolute zero, associated with the movement of charged particles within the object. EM radiation propagates as two orthogonal waves, with an electric and magnetic component, moving at right angles to the direction of wave propagation (Figure 2.1). These waves travel at a constant speed in a vacuum ($2.9979 \times 10^8\ \text{m s}^{-1}$) given by Maxwell's equation:

$$c = \frac{1}{\sqrt{\epsilon_0 \mu_0}} \quad (2.1)$$

where c is the speed of light in a vacuum; ϵ_0 is the permittivity (the ability to polarize in response to an

Table 2.1. Nomenclature of symbols used in this chapter.

<i>Symbol</i>	<i>Meaning</i>	<i>Value and units (variable units in parentheses)</i>	<i>Defined in equation</i>
c	Speed of light in a vacuum	$3.00 \times 10^8 \text{ m} \cdot \text{s}^{-1}$	2.1
ε_0	Permittivity of free space	$8.85 \times 10^{-12} \text{ F} \cdot \text{m}^{-1}$	2.1
μ_0	Permeability of free space	$1.26 \times 10^{-6} \text{ H} \cdot \text{m}^{-1}$	2.1
ν	Frequency	(Hz)	2.2
λ	Wavelength	(μm)	2.2
E	Energy	(J)	2.3
h	Planck's constant	$6.63 \times 10^{-34} \text{ J} \cdot \text{s}$	2.3
$B_\lambda(T)$	Blackbody radiance	($\text{W} \cdot \text{m}^{-2} \cdot \mu\text{m}^{-1} \cdot \text{sr}^{-1}$)	2.4
K_B	Boltzmann constant	$1.38 \times 10^{-23} \text{ J} \cdot \text{K}^{-1}$	2.4
T	Temperature	(K)	2.4
λ_{max}	Maximum wavelength	(μm)	2.6
W	Wien's constant	$2,898 \mu\text{m} \cdot \text{K}$	2.6
π	Pi	3.14	2.7
σ	Stefan–Boltzmann constant	$5.67 \times 10^{-8} \text{ W m}^{-2} \text{ K}^{-4}$	2.7
α	Absorption coefficient	(m^{-1})	2.9
C	Concentration	($\text{mol} \cdot \text{m}^{-3}$)	2.9
l	Path length	(m)	2.9
I_{out}	Outgoing intensity	(W m^{-2})	2.9
I_{in}	Incoming intensity	(W m^{-2})	2.9
m	Refractive index	(unitless)	2.11
n	Real part of m	(unitless)	2.11
k	Imaginary part of m	(unitless)	2.11
ε	Emissivity	(unitless)	2.12
R	Reflectivity	(unitless)	2.12
F_{in}	Incident flux density	$\text{J} \cdot \text{Hz}^{-1} \text{ m}^{-2} \cdot \text{s}^{-1}$	2.13
θ_0	Incidence angle	(radians)	2.13
γ	Bistatic scattering coefficient	(unitless)	2.14
θ_1	Exitance angle	(radians)	2.14
Q_{EXT}	Extinction efficiency factor	(unitless)	2.16
C_{EXT}	Extinction cross-section	(unitless)	2.16

<i>Symbol</i>	<i>Meaning</i>	<i>Value and units (variable units in parentheses)</i>	<i>Defined in equation</i>
r	Particle radius	(μm)	2.16
F_{out}	Measured flux density	$\text{J} \cdot \text{Hz}^{-1} \cdot \text{m}^{-2} \cdot \text{s}^1$	2.17
l_a	Absorption length	(cm)	2.17
z	Height	(km)	2.17
γ_a	Absorption coefficient	(cm^{-1})	2.19
γ_s	Scattering coefficient	(cm^{-1})	2.20
F_+	Upward flux density	($\text{J} \cdot \text{Hz}^{-1} \cdot \text{m}^{-2} \cdot \text{s}^1$)	2.20
F_-	Downward flux density	($\text{J} \cdot \text{Hz}^{-1} \cdot \text{m}^{-2} \cdot \text{s}^1$)	2.20
L_f	Upwelling (forward) radiance	($\text{W} \cdot \text{m}^{-2} \cdot \mu\text{m}^{-1} \cdot \text{sr}^{-1}$)	2.22
J_f	Path-added (forward) radiance	($\text{W} \cdot \text{m}^{-2} \cdot \mu\text{m}^{-1} \cdot \text{sr}^{-1}$)	2.22
B_f	Blackbody (forward) radiance	($\text{W} \cdot \text{m}^{-2} \cdot \mu\text{m}^{-1} \cdot \text{sr}^{-1}$)	2.23
p	Pressure	(Pa)	2.24
H	Scale height	(km)	2.24
L_W	Non-specular radiance	($\text{W} \cdot \text{m}^{-2} \cdot \mu\text{m}^{-1} \cdot \text{sr}^{-1}$)	2.25
L_A	Radiance due to aerosol	($\text{W} \cdot \text{m}^{-2} \cdot \mu\text{m}^{-1} \cdot \text{sr}^{-1}$)	2.25
L_G	Specular radiance	($\text{W} \cdot \text{m}^{-2} \cdot \mu\text{m}^{-1} \cdot \text{sr}^{-1}$)	2.25
L_S	At-satellite radiance	($\text{W} \cdot \text{m}^{-2} \cdot \mu\text{m}^{-1} \cdot \text{sr}^{-1}$)	2.25
L_R	Rayleigh radiance	($\text{W} \cdot \text{m}^{-2} \cdot \mu\text{m}^{-1} \cdot \text{sr}^{-1}$)	2.25
t	Atmospheric transmission	(unitless)	2.25
μ	Cosine of satellite zenith angle	(unitless)	2.26
μ_0	Cosine of solar zenith angle	(unitless)	2.26
ω_0	Single scattering albedo	(unitless)	2.26
$p(\theta)$	Phase function	(unitless)	2.26
τ_A	Aerosol optical depth	(unitless)	2.26
β_{EXT}	Extinction coefficient	(m^{-1})	2.27

applied electric field) of free space; and μ_0 is the permeability (the ability to magnetize in response to an applied magnetic field) of free space.

These waves have many properties of interest for remote sensors. The most pertinent are the wave's *wavelength, frequency, amplitude, and energy*.

These descriptors provide fundamental information about how EM waves interact with matter (Section 2.4) and hence can be utilized (inversely) to yield information about the object of study.

Wavelength (λ) and frequency (ν) are most easily explained. If the wave is propagating at the

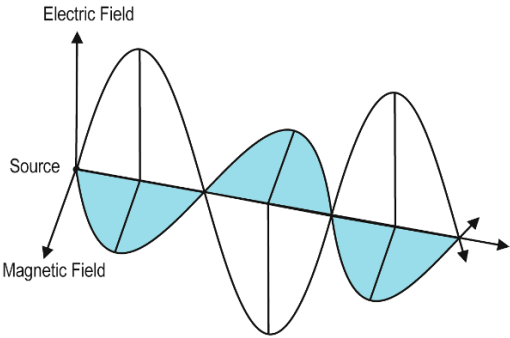


Figure 2.1. Propagation of plane-polarized electromagnetic waves.

speed of light in a given direction a certain number of peaks will pass past a stationary point over a given time interval. This is defined as the wave's frequency normally expressed in hertz (Hz) with units of oscillations per second. The wavelength of the radiation is defined as the inter-trough distance (Figure 2.2). These two properties are inversely related thus:

$$\nu = \frac{c}{\lambda} \quad (2.2)$$

The energy (E) of the wave is also related to the frequency (and thus wavelength) using the following formula:

$$E = h\nu \quad (2.3)$$

where h is Planck's constant ($6.626 \times 10^{-34} \text{ J} \cdot \text{s}$).

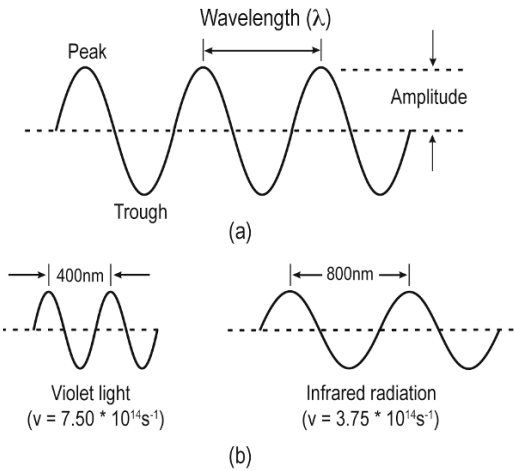


Figure 2.2. The relationship between frequency and wavelength.

Hence the amount of energy is directly proportional to the frequency and inversely proportional to the wavelength of the radiation. The entire range of possible electromagnetic energy constitutes the electromagnetic spectrum (also known as the EM spectrum or simply spectrum) (Figure 2.3). The spectrum is divided into wavelength regions with specific nomenclature. Though for most parts of the spectrum there is a general agreement on the boundaries and nomenclature of the regions and subregions, the infrared portion of the spectrum is one where there is considerable debate and little

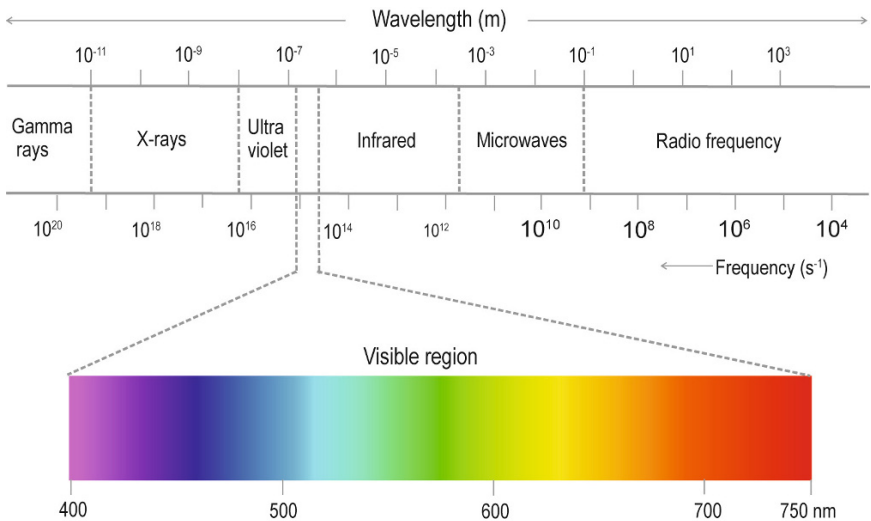


Figure 2.3. The electromagnetic spectrum.

Table 2.2. Regions of the electromagnetic spectrum.

Region	Sub-region	Popular acronym	Wavelength ranges
Gamma ray		Gamma	<0.03 nm
X-ray			0.03–30 nm
Ultraviolet		UV	0.3–0.4 mm
Visible		VIS	0.4–0.7 mm
Infrared	Near-infrared	NIR	0.7–1.3 μm
	Shortwave infrared	SWIR	1.3–3.0 μm
	Mid-infrared	MIR	3.0–8.0 μm
	Thermal infrared	TIR	8.0–14 μm
Microwave	K band		0.8–2.4 cm
	X band		2.4–3.8 cm
	C band		3.8–7.5 cm
	S band		7.5–15 cm
	L band		15.0–30.0 cm
	P band		30.0–100 cm
Radiowave			>100 cm

consensus. Throughout this book, we conform to the nomenclature given in Table 2.2.

It should be noted that, due to stratospheric ozone layer absorption, solar radiation near the Earth's surface has a short-wavelength limit at 0.29 μm (290 nm). Therefore, the region of the UV spectrum with an upper wavelength of about 290 nm is called solar-blind UV or blind UV. UV detectors with a long-wavelength cutoff below 290 nm are usually called solar-blind detectors.

In terms of remote sensing of volcanoes a range of wavelengths between 0.3 μm (3×10^{-7} m, the edge of the blind UV) and 1×10^6 μm (1 m, the far edge of the microwave region) is of special significance (see Chapter 5)

The generation of EM waves is a direct result of the oscillation of electric charge within matter. The oscillation occurs over a continuous range of frequencies and thus emits radiation at all wavelengths. However, radiation is not emitted equally at all wavelengths, rather it is distributed according to the object's emission spectrum. This spectrum

depends strongly on the temperature of the object and this interrelationship was determined by Max Planck in 1894. The discovery was aided by the concept of a *blackbody*, an object in thermal equilibrium with its surroundings that perfectly absorbs (see Section 2.4) and emits radiation. Planck was able to show that the intensity of radiation emitted by a blackbody varied with wavelength as a function of temperature as follows:

$$B_{\lambda}(T) = \frac{2hc^2}{\lambda^5 (e^{hc/\lambda K_B T} - 1)} \quad (2.4)$$

where $B_{\lambda}(T)$ is the blackbody radiance for a temperature (T); and K_B is the Boltzmann constant. Inverting the Planck function to solve for T shows that the higher the temperature the more energy is emitted at shorter wavelength (higher energy). This is also easily observed by plotting the emission spectra, derived from the Planck function, for objects of different temperature (Figure 2.4).

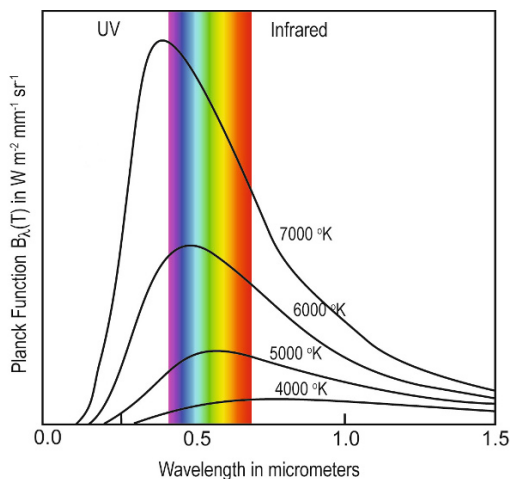
The position of the maximum in the emission spectrum is especially indicative of the relationship between wavelength and temperature and can be derived by setting the first derivative to zero (shown below):

$$\frac{\partial B_{\lambda}}{\partial \lambda} = 0 \quad (2.5)$$

which yields Wien's displacement law:

$$\lambda_{\max} = \frac{W}{T} \quad (2.6)$$

where W is Wien's constant (2,898 μm K).


Figure 2.4. Planck (blackbody) curves for objects of different temperature.

Using Wien's displacement law yields a peak in the Planck function of $0.5\mu\text{m}$ for an object at $5,870\text{ K}$ (the temperature of the surface of the Sun) and $10.0\mu\text{m}$ for an object at 290 K (a temperature representative of the Earth's surface). This shows that the peak of the Sun's emitted radiation falls in the visible region of the EM spectrum, and the peak of Earth's emitted radiation falls in the thermal infrared region of the EM spectrum. It also shows that the Sun is emitting greater amounts of high-energy radiation relative to the Earth, because it is hotter.

It can also be observed in Figure 2.4 that the hotter an object is the more radiation it emits in total. The amount of energy emitted by an object of a given temperature over all wavelengths is described by the Stefan–Boltzmann equation, the integration of the Planck function with respect to wavelength:

$$B(T) = \int_0^\infty B_\lambda(T) d\lambda = \frac{\sigma}{\pi} T^4 \quad (2.7)$$

where σ is the Stefan–Boltzmann constant ($5.67 \times 10^{-8} \text{ W m}^{-2} \text{ K}^{-4}$).

This relationship indicates that the amount of energy emitted is extremely sensitive to the temperature of the object. In the case of the Sun and the Earth, an equivalent area of the Sun is emitting nearly 160,000 times as much radiation as the Earth.

2.3 INTRODUCTION TO REMOTE SENSING

2.3.1 Inverse problems

Mathematical solutions can be divided into two distinct types: forward and inverse. A simple thought experiment, involving a new species of animal, helps elucidate the differing rationales, issues, and limitations of each type. Given a complete knowledge of the animal (its height, weight distribution, skeletal structure, speed of motion, etc.) and of the ground upon which it walks (moisture content, compressibility, softness, etc.) a perfectly accurate prediction of the tracks of the animal can be made. This is a classic forward solution. The problem is well constrained and perfect knowledge of the system yields an exactly accurate result.

The inverse analog to this problem is, upon finding the tracks, deriving what the animal looked

like. Here the issues associated with inverse solution become obvious. The distance between the footprints is a function of the size of the animal and the speed at which it was traveling. Given no a priori information about the animal it is impossible to derive a unique solution to the question “how fast was the animal traveling?” The problem is ill-constrained. In this case there is one piece of information and two variables, producing not one but a suite of possible combinations of answers.

Remote sensing, by its very nature, is a study of inverse problems. As opposed to conventional field-based temperature measurement (e.g., using mercury thermometers or probes), in remote sensing the sensor does not make physical contact with the ground. Instead the temperature is derived from the amount of radiation leaving the ground, which is a function of temperature and wavelength (see Section 2.3.2 for a more complete overview). However, there are many caveats to this calculation. The amount of radiation emitted by the ground is also modulated by its emissivity (a description of the efficiency of the ground to emit). This radiation also has to travel through the atmosphere to the sensor and is therefore a complex descriptor of the ground's behavior and the composition of the atmosphere. Only by decoupling these effects can the true ground temperature be accurately determined.

2.3.2 Modes of remote sensing

Active and passive techniques are used to acquire information about the Earth's surface and/or the atmosphere by the interaction of radiation with matter. An active technique involves the generation of energy and capture of its returning signal, after having undergone some transformation. Passive remote sensing is the acquisition of radiation being produced without instrumental stimulation and records natural emission or reflection from the target. A radar system, whose sensor both transmits and receives radiation, is an example of an active sensor. An infrared instrument, simply collecting radiation being produced by a target due to its own temperature, without additional experimental stimulation, is an example of a passive sensor.

2.3.3 Platforms and orbit types

Several types of orbits exist that can be used to address different scientific issues. The two most commonly used orbits are geostationary or geosyn-

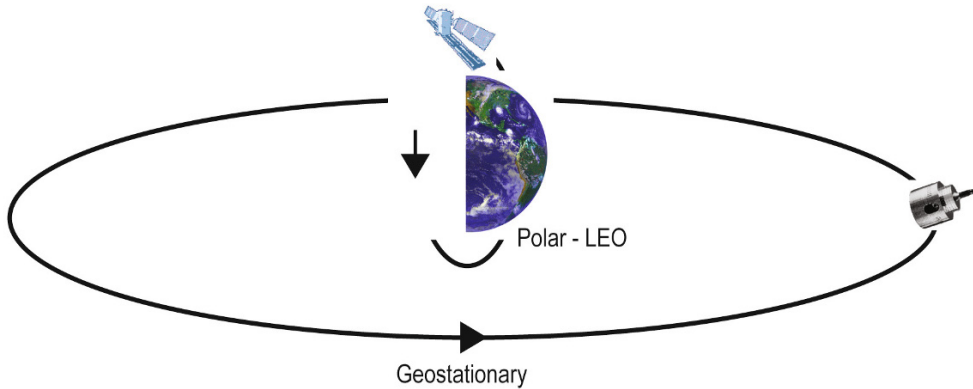


Figure 2.5. Geostationary and low Earth orbits.

chronous (GEO) and low Earth orbit (LEO) (Figure 2.5). Both have advantages and disadvantages in terms of the resolutions of the images acquired (see Section 2.3.4 for a more complete description of types of resolution and their interrelationships).

A geostationary orbit can be defined as an orbit at the distance required to keep the satellite stationary (in the Earth's frame of reference) above a single point above the equator. This is achieved by having an orbital period (the amount of time it takes to make a single orbit of the Earth) of exactly the same time as the period of a single rotation of the Earth. The distance required to achieve this orbit (from the Earth's surface) is approximately 35,800 km above mean sea level. Applications of these types of orbits include satellites designed to study large-scale systems at short intervals, such as weather satellites. Examples used by volcanologists are the GOES (Geostationary Operational Environmental Satellites) suite to observe drifting volcanic ash clouds (e.g., Ellrod and Schreiner, 2004) and thermal anomalies (Harris *et al.*, 2001).

LEO can be further subdivided into two orbit types based on their inclination relative to the poles. A polar orbit is one with an inclination of 90° . This orbit has the advantage of being able to acquire an image of almost every point on the Earth's surface. If the inclination of the orbit changes then the northernmost and southernmost parts of the globe become inaccessible. This is called the terminator effect. This is sometimes preferential, as in a near-polar, Sun-synchronous type orbit where the orbital plane of the satellite precesses (rotates) slightly to keep pace with the Earth's revolution around the Sun. This has the effect of making the satellite cross any given point on the orbit at roughly the same

time each day. This becomes important when the object of study has diurnal temporal dependence (e.g., relative humidity) or if, as in the case of Radarsat, the instrument is partially powered by solar panels that need to be constantly pointed at the Sun. Most Earth-observing satellites are therefore designed to have near-polar, Sun-synchronous LEOs, and strictly polar orbits are practically never used. LEO sensors are heavily used by volcanologists; for example, to map lava flows using Landsat (Oppenheimer, 1991) or to quantify volcanic emissions using MODIS (Watson *et al.*, 2004).

2.3.4 Spatial, temporal, and spectral resolution

Resolution refers to the resolvable limit of a system and can be broadly described as a measure of the system's accuracy. In the context of spatial, temporal, and spectral resolution, satellite data resolution can be defined using the minimum distance, time, and wavelength range covered by the satellite sensor.

The spatial resolution of a sensor is a measure of the smallest angular or linear separation between two objects that can be resolved by sensor. In a digital image, the resolution is limited by the pixel size (i.e., the smallest resolvable object cannot be smaller than the pixel size). The pixel size is determined by the sampling distance. Image resolution and pixel size are often used interchangeably. In reality, they are not equivalent. An image sampled at a small pixel size does not necessarily have a high resolution. If an instrument has a spatial resolution of 10 m, then no objects smaller than 10×10 m can

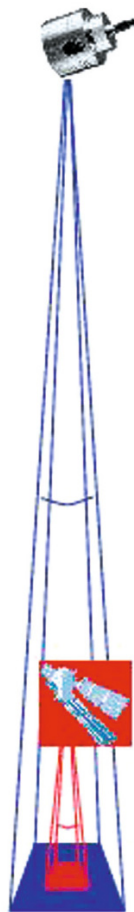


Figure 2.6. Instantaneous field of view and spatial resolution.

be distinguished from their background. This does not necessarily mean they cannot be *detected*. If the spatial resolution doubles (i.e., becomes 5 m), the image data volume increases by a factor of 4. Spatial resolution is a function of the distance from the Earth's surface and the instantaneous field of view (IFOV) of the instrument (Figure 2.6).

The temporal resolution of the instrument is a function of the repeat time; that is, the time it takes to re-acquire an image of the same point on the Earth's surface. For a geostationary orbit this is simply determined by the speed at which the data can be transferred to a receiving station and the memory of the recorder cleared. This is typically on the order of a few tens of minutes. At the other extreme a LEO satellite with a narrow swath width

might have a repeat time on the order of 15 days (typical) to several months (to give an extremely dense network of nadir tracks).

The spectral resolution of the instrument is characterized by the range of wavelengths over which a single measurement is acquired. It is a function of the width of the channel (in units of wavelength) encompassed by a measurement and the distance between the center points of separate channels. A broad single channel constitutes a pan-chromatic band (i.e., encompasses a significant range of wavelengths). An instrument with several discrete channels (typically on the order of 0.5–1.0 μm wide for an IR instrument) can be described as multispectral. As the number of channels increase and the spectral bandwidth of individual channels reduce (finer/higher spectral resolution), we transition from multispectral sensors to hyperspectral sensors.

The three different resolutions are not completely independent. Spatial resolution is strongly inversely related to temporal resolution, wavelength, and spectral resolution. The first relationship is somewhat obvious, the second and third less so. It can be shown that the spatial resolution of the instrument is a function of the distance to the target. The farther away the sensor is from the target the less detail can be resolved (Figure 2.6). For example, a car's license plate can be easily read by most people using the naked eye at a distance of 1 m and by no one at a distance of 1 km.

The relationship between wavelength and spatial resolution is defined by the diffraction limit of a finite aperture. Because any system's optical dimensions are in some way constrained it can be shown that angular resolution can be approximated by λ/D , where λ is the wavelength and D is the diameter of the aperture or lens. This phenomenon is best detailed in two examples (after Rees, 2001). First, consider a visible sensor 1,000 km above the surface of the Earth detecting radiation at 0.5 μm through a lens 5 cm in diameter. Using diffraction approximation it can be derived that the angular resolution is limited to about 10^{-5} radians or a spatial resolution of about 10 m. In contrast a passive microwave radiometer might have an antenna 1 m in diameter detecting radiation of 3 cm wavelength. At the same altitude (1,000 km) this would yield an angular resolution of 3×10^{-2} radians and a spatial resolution of 30 km. There are ways to circumvent the aperture limit (such as synthetic aperture radar) which are discussed in Chapter 8, but beyond the scope of this chapter.

2.4 RADIATIVE TRANSFER AND ATMOSPHERIC WINDOWS

2.4.1 Definitions

In order to ground the reader in an understanding of the behavior of radiation it is helpful to start with a series of definitions and interrelationships between the different ways EM radiation can interact with matter (Figure 2.7). The following is a series of simple definitions of the potential outcomes of radiation/matter interaction.

Absorption can be defined as the interaction of matter with radiation where a change in quantized energy level is observed. Absorption is the inter-

action of radiation with the dipolar structure of the target in a number of different regimes of varying energy based upon the bonding of the target's molecular structure. The energy absorbed by the target is typically emitted at longer wavelengths.

Emission describes the EM radiation given out (emitted) by a target material due to its thermal state. This is a function of the temperature of the object (Planck's Law, see Section 2.2.1) and the ability of the material to absorb, emit, and reflect radiation. In general the hotter the object the more radiation (in total) it will emit, and that emitted energy will be at lower wavelength. Emission occurs in all directions.

Scattering is a description of the interaction of EM radiation with atoms, molecules, and particles where the wavelength of the radiation is unaffected (given we make the assumption that the scattering is *elastic* and ignore fluorescence) but the exitance angle is a function of the target's size, composition, and roughness. The term scattering is typically, though not exclusively, applied to atmospheric constituents; if the radiation is redirected by a surface then it is termed reflection.

Reflection describes the redirection of radiation by a surface. Again the wavelength of the radiation is unaffected. The roughness of the surface dictates the angles at which the radiation leaves the target. Note that a surface may not be uniformly rough at all wavelength scales. For a perfectly smooth target the incident angle (θ_1) is equal to the exitance angle (θ_2).

Refraction is the interaction of radiation at a surface or boundary. One conceptual idea (offered by Huygens) is that EM radiation travels at different speeds through different materials, and it is this action across the boundary that ultimately alters the direction of propagation. The ratio of the sine of the incident angle (θ_1) to propagation angle (refraction angle, θ_2) is equal to the ratio of speed in which the wave propagates through the two media.

Transmission is the lack of attenuation of EM radiation. Transmitted radiation appears to pass unscathed (in terms of intensity and wavelength) through the target. As per the concept of total energy (i.e., the total amount of radiation must sum to 1), the following relationships can be used to describe the transfer of radiation. Note that two general descriptors of the prevention of EM radiation reaching a sensor are *extinction* and *attenuation*, the sum of the processes of absorption

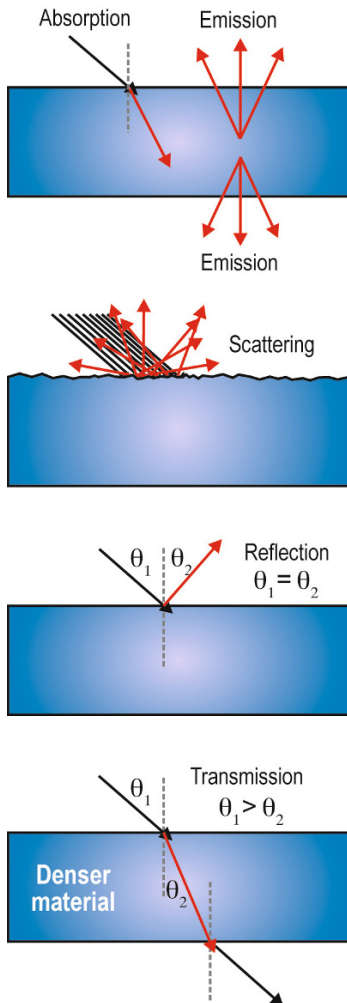


Figure 2.7. Energy-matter interaction.

and scattering:

$$\left. \begin{array}{l} (a) \ 1 = \text{absorption} + \text{scattering} + \text{transmission} \\ (b) \ \text{transmission} = 1 - \text{emission} + \text{scattering} \\ (c) \ \text{absorption} + \text{scattering} = \text{extinction} \\ (d) \ \text{transmission} = 1 - \text{extinction} \end{array} \right\} (2.8)$$

2.4.2 Interaction of radiation with matter

Energy from EM radiation cannot be destroyed (rule of the conservation of energy), only converted into a number of different states of increased energy within the target, or the wave can be deflected (in the case of scattering and reflection) and no energy transferred to the target.

The radiation attenuated (prevented from passing through the target and leaving at the same angle) can be detected as a reduction in path radiation according to the Beer–Bouguer–Lambert Law:

$$I_{\text{out}} = I_{\text{in}} e^{-\alpha c l} \quad (2.9)$$

The attenuation signal is then a function of the medium's ability to attenuate radiation of a given wavelength (α), the concentration of the medium (c), and its path length (l) (see also Figure 2.8). In the context of remote sensing of the Earth's surface I_{in} is the variable of interest and the exponents need to be taken into account to get an accurate description of the surface-leaving radiance (called atmospheric correction: Section 2.5). If the atmosphere itself is the target of interest then I_{in} is either known or estimated and the exponents (either singularly or collectively) are the variables of interest.

The three main processes by which radiation can be modified by the target will now be discussed in more detail. These are absorption, emission, and reflection/scattering. At thermal equilibrium absorption (coefficient α) and emission (E) are inextricably linked through Kirchhoff's Law:

$$E_{\lambda} = \alpha_{\lambda} B_{\lambda}(T) \quad (2.10)$$

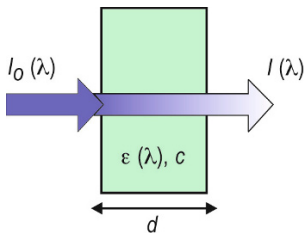


Figure 2.8. Beer–Bouguer–Lambert Law.

The fact that the absorption coefficient α is a function of wavelength is of great importance when discussing absorption and emission. The frequency (proportional to $1/\lambda$) of incident EM radiation controls what type of absorptive interaction with the target occurs. The higher the frequency the greater the energy associated with that wave and the more energetic the excitation caused by the wave–matter interaction. For example, visible radiation at a frequency of 4.3×10^{14} – 7.5×10^{14} Hz (0.4–0.7 μm wavelength) causes changes in the configuration of electrons, specifically the orbital configuration of outer (valent) shell electrons. In comparison microwave energy with a frequency of 1×10^{11} Hz (1,000 μm) alters the way in which the target's molecules rotate. Rotational energy levels are closer together than electronic transitional energy levels and hence require EM radiation of less energy to change their state. A complete picture of which molecular mechanisms are associated with which frequencies (and wavelengths) can be seen in Figure 2.9. Note that as we are currently considering molecular interactions, the situation becomes much more complex for rigid media (e.g., solids).

The emission spectrum of a target is governed to a first order by the temperature of the target (Equation 2.4) if the target approximates a blackbody emitter. Most objects in nature do not, and their emission spectra are a complex function of the blackbody curve and the emissivity of the target. A simple thermodynamic argument can be invoked to suggest that if the target is in thermal equilibrium then it must be absorbing and emitting at the same rate (called Kirchhoff's Law). The emissivity of the material is governed by its refractive index, a wavelength-dependent complex number (m) of the form:

$$m = n + ki \quad (2.11)$$

The real part of the refractive index (n) describes the reflective properties of the material, and the imaginary part (k) relates to the absorptive properties.

According to Kirchhoff's law, absorption equals emission; it can therefore be deduced that the emissivity (ϵ) of an opaque surface can also be defined, as a consequence of the equation scheme (2.8) as:

$$\epsilon = 1 - R \quad (2.12)$$

Reflection and reflectivity (R) illustrate the scattering of radiation by a surface (as opposed to scattering which is a term normally reserved for the interaction of radiation with atmospheric gases

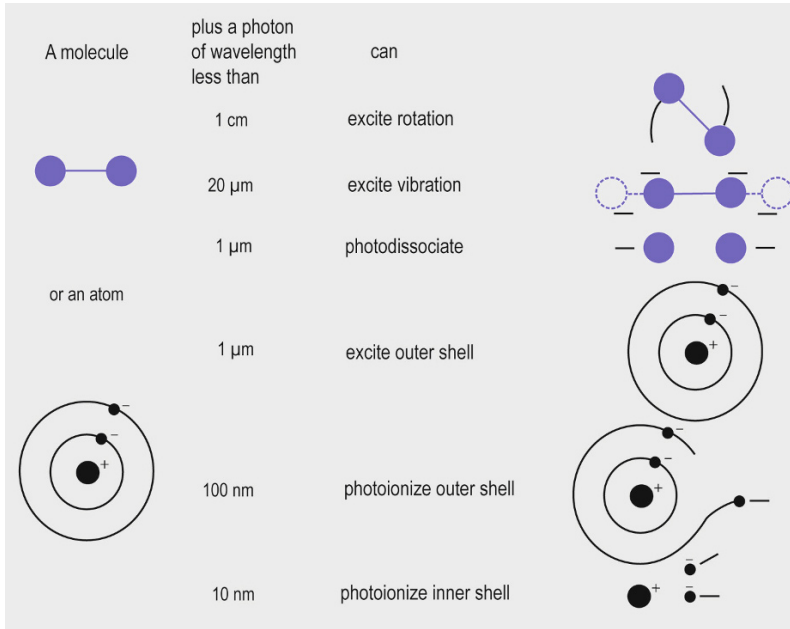


Figure 2.9. The relationship between energy and transition type.

and particles). These terms are, in reality, interchangeable and bridged by a third term, albedo. Both surfaces, such as snowpack, and aerosols, such as clouds, can be defined in terms of their albedo.

Again, the reflectivity is somewhat controlled by the refractive index, specifically (n) the real (non-imaginary) part in Equation (2.11). If a surface is opaque it can be assumed that all the radiation that is not absorbed is reflected. For a perfectly flat surface a simple description, called specular reflectance, can be assumed, where the exitance angle of the radiation is simply equal to the angle of incidence. The other end member of scattering is called Lambertian scattering, where the surface is *ideally* rough so that the incoming radiation is scattered equally in all directions.

Clearly, most surfaces are neither specular nor Lambertian but somewhere in between. This type of scattering is called non-specular, of which Lambertian is a specific and unrealistic end member. In fact, as seen in Section 2.5.2, scattering can be modeled simply as the sum of specular and non-specular reflection. Another useful descriptor is the bidirectional reflection function or BDRF defined as:

$$\text{BDRF} = \pi I_{\text{out}} / F_{\text{in}} \cos \theta_0 \quad (2.13)$$

where I_{out} is the intensity of reflected radiation; F_{in}

is the incident flux density; and θ_0 is the angle of incidence.

In radar systems BDRF is normally replaced by the *bistatic scattering coefficient* (γ):

$$\gamma = (\text{BDRF}) 4\pi \cos \theta_1 \quad (2.14)$$

where θ_1 is the angle between the outgoing radiation and a plane line normal to the surface.

The basic principles of scattering apply equally to reflectance. As an example, the green color of the leaves of a tree is a function of the reflectivity of the leaf. This in turn is explained by the absorption of visible light by chlorophyll pigments in the leaf. Chlorophyll absorbs strongly in all regions of the visible spectrum. However, chlorophyll absorbs slightly less strongly at the wavelength of green light, relative to other wavelengths. As a ramification of Equation (2.12) this means that green light is most reflected hence the leaf appears green.

Scattering of radiation by atmospheric constituents have an additional level of complexity when compared with a solely absorptive regime. It is a function of wavelength, scatterer size, and the angle of the incoming radiation. The mechanisms for scattering are complex and can be subdivided into three categories as a function of the ratio between the size of the scatterer and the wavelength of inci-

dent light. If the scatterer's diameter is much, much less than the wavelength of incident light then the scattering that occurs can be described using the Rayleigh scattering formula:

$$I_{\text{out}} = I_{\text{in}}[1 + \cos^2 \theta_0] \left(\frac{1}{\lambda}\right)^4 |\psi|^2 / r_p^2 \quad (2.15)$$

where ψ is the polarizability; and r_p is the distance to the particle.

This is most robustly applied to scatterers with a single oscillating dipole and indicates that scattering increases strongly as wavelength decreases. This has commonly observable ramifications including the color of the sky. The sky appears blue because N_2 and O_2 molecules in the atmosphere scatter shorter wavelengths (i.e., blue light) more than longer wavelengths from the plane of incidence. In the Rayleigh regime, light is strongly scattered at all angles relative to the angle of incidence.

The next regime (Mie scattering) occurs as the scatterer's diameter approaches the wavelength of incident light, the region where scattering is strongest. The mathematic theory is more complex than in the Rayleigh regime and the derivation of Mie scattering theory is well beyond the scope of this chapter. As a general rule, however, the larger the particle the more complicated the pattern of scattered light and the more the scattering occurs in the forward direction, until non-selective scattering (see below) predominates.

A convenient way to consider the theory is in the context of the scattering cross-section, a critical

component of the Mie derivation. The scattering cross-section represents the size of the particle required to cause the attenuation calculated if simply the geometric area is considered. Hence the extinction efficiency factor is related to the scattering cross-section thus:

$$Q_{\text{EXT}} = \frac{C_{\text{EXT}}}{\pi r^2} \quad (2.16)$$

where Q_{EXT} is the extinction efficiency factor, defined as the ratio between the extinction cross-section (C_{EXT}) and the geometric area of a particle with radius r .

Plotting the extinction efficiency factor against the size parameter $X(2\pi r/\lambda)$ is instructive in understanding the relationship within the different regimes (Figure 2.10). Here the different scattering regions are clearly delimited. As X tends towards 1 the extinction efficiency factor increases approximately as to $1/\lambda^4$ (from Rayleigh scattering theory). At the edge of the Mie region the situation becomes more complex with the addition of large-scale and small-scale oscillations. It is the presence of the edges of particles and their complex interaction that becomes increasingly important. It is the behavior of complex interference patterns that underpins Mie theory.

Rather counterintuitively the extinction efficiency factor tends towards 2 as the ratio r/λ increases into the third scattering regime, the non-selective regime past the large particle limit. Here the extinction efficiency factor is clearly independent of the r/λ ratio and remains at 2 because no

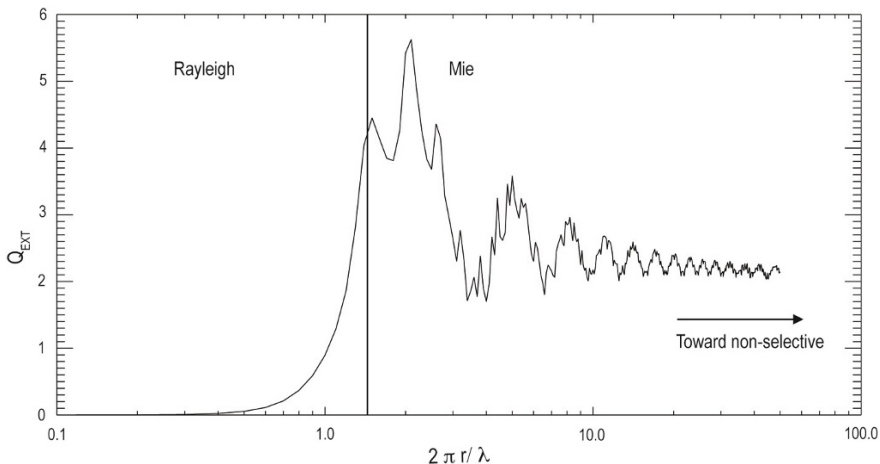


Figure 2.10. Plot of Q_{EXT} vs. $X(2\pi r/\lambda)$ showing Rayleigh, Mie, and non-selective scattering regimes for an andesite ash particle of $4\ \mu\text{m}$ radius.

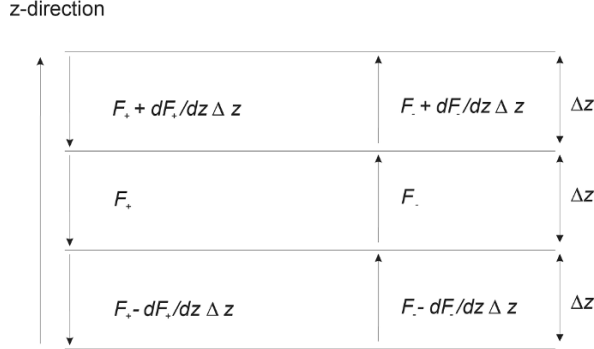


Figure 2.11. Three-slab radiative transfer model (after Rees, 2001).

matter how large particles become they still exhibit edge effects. The physical ramifications of a change of regime (from Mie to non-selective scattering) are observable in the natural world. Clouds appear white due to non-selective scattering of visible light by large ($>50\ \mu\text{m}$) particles whereas sunsets are oranges and reds as the shorter wavelengths of visible light are removed by smaller atmospheric particles ($<10\ \mu\text{m}$) through Mie scattering.

2.4.3 The radiative transfer equation

The previously described conceptual framework can be represented in a single mathematical form by the radiative transfer equation. The term transfer implies the propagation of radiation from one place to another. In order to discuss the radiative transfer equation in detail a physical framework of an atmosphere of several parallel slabs needs to be invoked (Figure 2.11). Here radiation can be seen to propagate to and from any of the three layers into adjacent layers.

Using the theoretic framework suggested by Rees (2001), it can be shown, from the starting point, that the density of flux (F) varies according to

$$F_{\text{out}} = F_{\text{in}} \exp\left(-\frac{z}{l_a}\right) \quad (2.17)$$

where F_{out} is the exitant flux; z is the distance (in the case of the atmosphere, height); and l_a is the absorption length coefficient and hence

$$\frac{dF}{dz} = -\frac{F}{l_a} \quad (2.18)$$

where

$$\gamma_a = \frac{1}{l_a} \quad (2.19)$$

where γ_a is the absorption coefficient.

It can be shown, given that we assume that absorption occurs in the $+z$ direction and scattering occurs only in the $-z$ direction, that the flux of radiation propagating in the forward direction through the middle slab can be described in terms of the transmission of radiation from the level below and backscattering from the level above. This can be mathematically defined as:

$$\frac{dF_+}{dz} = -(\gamma_a + \gamma_s)F_+ + \gamma_s F_- \quad (2.20)$$

where F_+ is the flux density in the $+z$ direction; F_- is the flux density in the $-z$ direction; and γ_s is the scattering coefficient.

Correspondingly the backward traveling radiation in the slab can be defined as

$$\frac{dF_-}{dz} = (\gamma_a + \gamma_s)F_+ - \gamma_s F_- \quad (2.21)$$

In order to determine the radiative transfer over three dimensions (i.e., something approximating reality) we have to move from the change in flux from one slab to another to a change in radiance. This nomenclature takes into account the fact that only considering backward scattering is a gross oversimplification. Conventionally this is done with consideration of frequency rather than wavelength. Equation (2.20) can be converted to consideration of radiance thus:

$$\frac{dL_f}{dz} = -(\gamma_a + \gamma_s)L_f + \gamma_s J_f \quad (2.22)$$

where L_f and J_f are the forward-propagating and path-added (by scattering) radiances.

Addition of an emission term yields a complete full description of radiative transfer in the $+z$

direction:

$$\frac{dL_f}{dz} = -(\gamma_a + \gamma_s)L_f + \gamma_s J_f + \gamma_a B_f \quad (2.23)$$

where B_f is the blackbody (Planck) spectral radiance of an object with temperature T .

It is important to note that the sum of the absorption and scattering coefficients is important in the radiative transfer equation. The ratio of the coefficients is critical in understanding the way a material will appear. Typically, highly particulate materials, such as clouds, appear white as the scattering coefficient overwhelms the absorption coefficient, due to the fact that the scattering coefficient is dependent on the number of particle surfaces,

whereas the absorption coefficient is not, allowing scattering to dominate.

2.4.4 The atmosphere

Knowledge of the atmosphere is important in all satellite remote sensing. Either the atmosphere is the subject of study or the effects of the atmosphere require careful removal before information about the surface can be accurately determined. The pressure profile and the vertical chemical and temperature structure of the atmosphere control its radiative effects and will be briefly described here for completeness.

The vertical temperature profile of the atmosphere has been used in the past to delimit regions

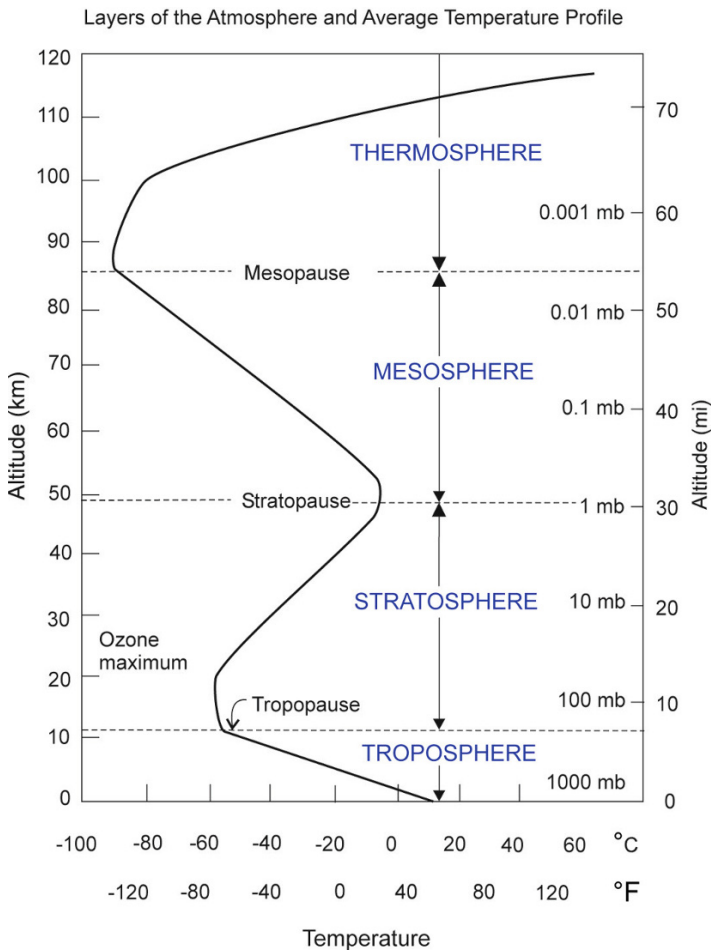


Figure 2.12a. Vertical structure of the atmosphere with respect to temperature.

of the atmosphere (Figure 2.12a). The lowest part of the atmosphere, the troposphere, is a well-mixed and turbulent regime with a negative temperature gradient (lapse rate) with increasing height. Above the troposphere is the stratosphere, a much drier layer with little vertical mixing with increasing temperature with altitude. The tropopause is the first point of inflection in the temperature profile and provides an effective boundary to all but the most buoyant air parcels. Above the stratosphere (and separated by the stratopause) is the mesosphere, another region of negative lapse rate. Above that is a second inflection (the mesopause) and another region with a positive temperature gradient, the thermosphere. In terms of volcano remote sensing, including both removal of atmospheric effects to

accurately quantify surficial products and detection of subaerial emissions, the troposphere and stratosphere are the most significant regions.

The pressure structure of the atmosphere (Figure 2.12b) is much more straightforward. Pressure decreases exponentially as a function of height and can be approximated thus

$$p(z) = p(0)e^{-z/H} \quad (2.24)$$

where p is the pressure; and H is the scale height (approximately 8 km of the troposphere).

Two ramifications of this equation are that half the mass of the atmosphere lies beneath a height of 5.5 km and 99% of the atmosphere is contained within the bottom 30 km.

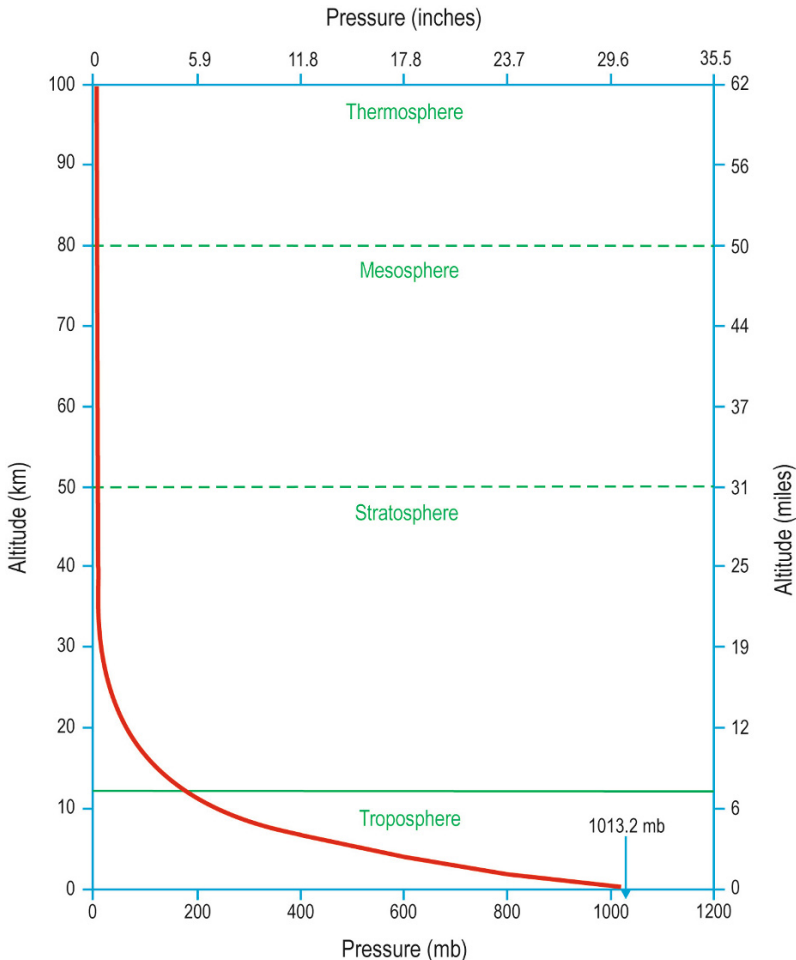


Figure 2.12b. Vertical structure of the atmosphere with respect to pressure.

The atmosphere is made up mostly of N_2 and O_2 making up 99% of the atmosphere (78% and 21%, respectively). Nitrogen is chemically and radiatively unreactive and the concentration of O_2 varies as a function of pressure. Ignoring water vapor for the moment the next two most abundant gases (Ar and CO_2) also vary as a simple function of altitude. A radiative model of the atmosphere based on these four species (>99% of the atmosphere) would actually be relatively straightforward.

It is the highly variable species, particularly H_2O and O_3 , that add the complexity in the way the atmosphere behaves radiatively. O_3 , for example, varies with altitude as a function of the UV radiation and O_2 required to make it. O_3 exists in a layer with a peak concentration at about 35 km because above this boundary there is not enough O_2 and below there is not enough UV radiation (it is strongly attenuated by the atmosphere). H_2O is even more complicated. Not only does the concentration of water vapor vary on almost every scale upon which it can be measured, it is also spectrally spectacularly complex. In terms of correcting the surface-leaving radiance for the effects of the atmosphere, understanding the vertical distribution of water vapor (also the most variable of all atmospheric species) is most critical.

2.4.5 Atmospheric windows

The atmosphere plays a vital role in the global Earth system and is studied extensively using remote-sensing techniques. Volcanic contributions, such as ash (Chapter 5) and gases (Chapter 6), perturb the atmosphere and affect the radiative transfer (and hence, potentially, climate) of the

atmosphere. Study of surficial volcanic products also requires an understanding of the atmosphere and its radiative effects. In either case the transparency of the atmosphere is critical in facilitating effective remote sensing. The atmosphere is made up of a series of wavelength regions of higher atmospheric transmission (Figure 2.13) which are targeted when the position of a satellite sensor's channels are being decided. In general, radiation of wavelengths above 10 mm are transmitted through the atmosphere and radiation below $0.3 \mu m$ is not. A second region of high opacity exists between $20 \mu m$ and 2 mm. The remaining regions, particularly those between 0.3 and $20 \mu m$ are complex and highly variable over short-wavelength ranges (Figure 2.13). The regions of high transmission are called "atmospheric windows" as they permit study of the Earth's surface (or the lower atmosphere) from space.

2.5 ATMOSPHERIC CORRECTION

Even though the atmosphere is relatively transparent at the wavelengths at which most satellite sensors operate, the atmosphere still contributes significantly to the at-satellite radiance. Whether the object of study is subaerial emissions of ash or pyroclastic deposits, correction of the detected radiance for the presence of the atmosphere is vital. This can be undertaken in a number of ways that can be binned into three categories. Empirical, or image-based techniques, determine the contribution of the atmosphere to the signal using information contained within the image only. Second, ground truthing can be used to determine the effects of the

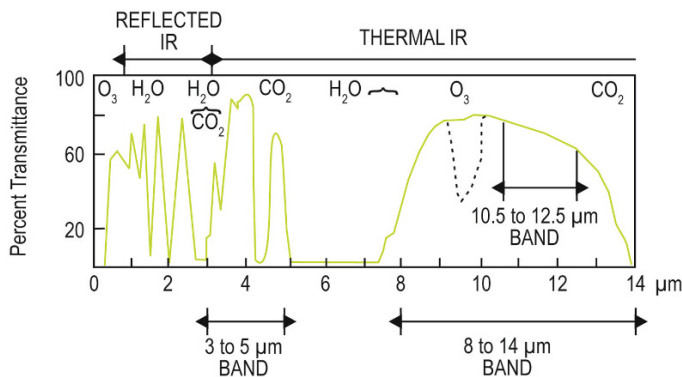


Figure 2.13. Atmospheric windows.

atmosphere by indicating what a known target would look like without the presence of an atmosphere. Third, radiative transfer models use external information about the atmosphere, specifically its vertical temperature and pressure and water vapor profile, to calculate (and hence remove) the contribution of the atmosphere.

There are advantages to all types of atmospheric corrections. Empirical techniques do not require external information, are computationally cheap, and can be undertaken simply with the image under study. Ground truthing offers an inexpensive solution that provides a quantitative and accurate solution. Modeling techniques are most robust and provide information about radiative transfer in the vertical profile, rather than a single column-averaged value.

2.5.1 Using empirical techniques and ground truthing

Intra-image atmospheric correction techniques vary depending on the wavelength range of the spectral bands of the image. As previously discussed, radiation at shorter wavelengths in the 0.3–20 μm range are much more highly scattered relative to longer wavelengths. The near UV, visible, and near IR can be considered scattering only regimes. For longer wavelengths the opposite holds true. For radiation $>8\mu\text{m}$ the atmosphere can be considered almost exclusively absorptive. Intermediate wavelengths, particularly the SWIR, must have a complete model of both scattering and absorption by the atmosphere. In short, reflected solar radiation is more likely to be mostly scattered in the atmosphere and emitted terrestrial radiation is more likely to be absorbed.

In the VNIR reflective regime the contribution of the atmosphere is likely to be a brightening of the image as incoming solar radiation is backscattered by the atmosphere before reaching the Earth. This path-added scattering explains why the horizon at distance has a paler appearance than similar features in the mid-ground and foreground. The reflectance contribution of the atmosphere can be derived using ground truthing and image-based techniques. Ground truthing involves selecting a target, typically dark in the NIR (such as a water body) and taking ground-based measurements of the reflectance of the target at some small distance above the target (on the order of centimeters to meters). This reflectance can then be assumed to truly represent the reflectance of the target, and the difference

between that measurement and the at-satellite reflectance is the contribution of the atmosphere. Ground truthing should be undertaken at several targets within the image to correct for variations in the reflectance associated with the angular dependence of scattering in the atmosphere and must also consider, in the case of water, the angular dependence of reflection (including Sun glint) as well.

The dark-pixel correction attempts to address the same problem on a much simpler level. It assumes that the reflectance of this target is zero and that any radiative contribution is from the atmosphere. The atmospheric contribution can then be removed for every pixel in the image. This must be done for all bands and makes two fundamentally flawed assumptions: (i) the reflectance from the atmosphere is constant across the image; (ii) the atmospheric correction can be adequately considered as an additive effect. Problems also occur if calibration/validation is attempted using highly absorptive targets due to low signal-to-noise ratio.

In the absorptive regime the same options are provided. Ground truthing can be undertaken to correct for the absorption of ground-leaving radiance by the atmosphere, typically seen as a darkening of the image. Typically a bright, well-known, and homogeneous target is chosen and its emissivity characterized. Given knowledge of the target's temperature, the ground-leaving radiance can be derived. Again, the difference between ground-based and satellite measurements is a function of the atmospheric contribution. An additional option is multi-angle comparison. Because the emissive regime does not have a strong angular dependence the difference in at-satellite radiance from the same target at different angles can be assumed to be representative of the additional path length through which the target is being observed. Knowledge of the path length difference, derived from known quantities such as the angle of observation and the sensor altitude, can be used in conjunction with the two measurements to quantify the contribution of the atmosphere.

Image-based calculations typically involve a channel-differencing technique. As emissive measurements are mostly confounded by the presence of water vapor the channel-differencing technique normally focuses on this issue. One such example is the "split-window" technique (e.g., Wen and Rose, 1994). As well as being used to detect volcanic ash (Chapter 6) the split-window algorithm can be used to quantify the contribution of water vapor to

the brightness temperature—the temperature given by the blackbody (Planck) calculation ignoring emissivity and/or atmospheric effects—in the 11–12 μm region. The technique works well on homogeneous, isothermal surfaces of constant emissivity, such as the sea, and less well for complex land-based background.

2.5.2 Using radiative transfer models

Several radiative transfer models currently exist to facilitate accounting for the atmospheric effects on remote-sensing observations. Of these the LOWTRAN 7 and MODTRAN models are most commonly used. The models require a priori information about the constituents in the atmosphere and then propagate ground-leaving radiation to the sensor via a series of interconnected arbitrary atmospheric levels. Meteorological data from radiosondes are normally used to constrain the atmosphere in terms of the pressure, temperature, and relative humidity. Given accurate knowledge of the atmosphere, the radiative effects of the atmosphere can be derived from a forward solution of the mathematical framework of the radiative transfer equation (Section 2.4.3).

The presence of large amounts of atmospheric aerosol is likely to confound radiative transfer models. This can be addressed with an example where an atmospheric correction is required to remove the effects of an aerosol layer above a surface of interest (e.g., water). In the VNIR it can be shown that the at-satellite radiance is a function of both the surface and atmospheric contribution. This begins with an equation where the at-satellite radiance above a surface (L_S) is given by:

$$L_S = (L_W + L_G)t + L_R + L_A \quad (2.25)$$

where L_W and L_G are the non-specular and specular reflectance from the water, respectively; t is the transmittance of the atmosphere; L_R is path-added Rayleigh (molecular) scattering; and L_A is the path-added radiance due to aerosol scattering (the quantity of interest). L_W is normally small, at least for the VNIR. L_G can be estimated using the Sun–Earth–satellite geometry and surface roughness. It is almost negligible for all but a few viewing geometries. The single scattering approximation (SSA), rather than the multiple scattering scheme, should be used in the investigation of upwelling radiation from aerosols. The use of the SSA is justified by the fact that single scattering processes dominate the transfer of radiation in most atmospheric environ-

ments. The presence of high levels of multiple scatterers (typically clouds) normally negates the need for atmospheric correction at all. The SSA can be mathematically described thus.

$$L_A = \frac{\omega_0 \mu_0 F_0}{4(\mu + \mu_0)} p(\theta) \left\{ 1 - \exp \left[-\tau_A \left(\frac{1}{\mu} + \frac{1}{\mu_0} \right) \right] \right\} \quad (2.26)$$

τ_A is the optical depth due to aerosol scattering; ω_0 is the single scattering albedo; $\mu = \cos \theta^1$, where θ^1 is the satellite zenith angle; $\mu_0 = \cos \theta_{sza}$, where θ_{sza} is the solar zenith angle and $p(\theta)$ is the scattering phase function. Aerosol optical depth is calculated by integrating the extinction coefficient (β_{EXT}) with respect to height (z):

$$\tau_A = \int \beta_{\text{EXT}} dz \quad (2.27)$$

where the extinction coefficient is given by

$$\beta_{\text{EXT}} = \int \pi r^2 Q_{\text{EXT}}(m, r) n(r) dr \quad (2.28)$$

The calculation of Q_{EXT} is complicated and the theory behind the calculation is both lengthy and well documented elsewhere (Bohren and Huffman, 1983). Several scattering codes exist for the calculation of Q_{EXT} , and its analogues Q_{ABS} and Q_{SCA} .

Some of the parameters in Equations (2.26)–(2.28) can be determined by experiment or can be modeled mathematically to produce the most likely fit, as in the case of $p(\theta)$, the scattering phase function. Equation (2.26) is reduced by the small optical depth assumption:

$$(\tau_A [(1/\mu) + (1/\mu_0)] \ll 1) \quad (2.29)$$

to:

$$L_A \approx \frac{\omega_0 F_0}{4\mu} p(\theta) \tau_A \quad (2.30)$$

L_A can be plotted against τ_A and the slope calculated. Assuming ω_0 to be 1.0 then $p(\theta)$ is given by:

$$p(\theta) = \text{slope} \frac{4(\mu)}{F_0} \quad (2.31)$$

and $p(\theta)$ can be compared with known values as a validation.

Hence, from the at-satellite radiances of two images or one image with two view angles, an understanding of the radiative effects of the aerosol layer can be retrieved and the image can be corrected for the presence of the aerosol layer.

Table 2.3. Past and present missions used in the observation of volcanic emissions.

<i>Sensor name</i>	<i>Sensor acronym</i>	<i>Spectral region</i>	<i>Target</i>	<i>Reference</i>	<i>Year</i>
Atmospheric Infrared Sounder	AIRS	TIR	SO ₂ Ash Ice Lava flow	Carn <i>et al.</i> Wright <i>et al.</i> — Patrick <i>et al.</i>	2005 2005 — 2005
Advanced Spaceborne Thermal Emission and Reflection Radiometer	ASTER	TIR	SO ₂ Ice Ash	Henney <i>et al.</i> — —	In review — —
Advanced Very High Resolution Radiometer	AVHRR	TIR	Ash Ice	Dean <i>et al.</i> Guo <i>et al.</i>	2004 2004
Geostationary Operational Environmental Satellite	GOES	TIR	Ash Ice	Gu <i>et al.</i> Rose <i>et al.</i>	2005 2000
Global Ozone Monitoring Experiment	GOME	UV	SO ₂	Khokhar <i>et al.</i>	2005
Land Satellite	LANDSAT	VIS–TIR	Lava flow	Patrick <i>et al.</i>	2005
Microwave Limb Sounder	MLS	MW	SO ₂	Read <i>et al.</i>	1993
Moderate Resolution Imaging Spectroradiometer	MODIS	TIR	SO ₂ Ash Ice ThA	Watson <i>et al.</i> Watson <i>et al.</i> Watson <i>et al.</i> Patrick <i>et al.</i>	2004 2004 2004 2005
Ozone Monitoring Instrument	OMI	UV	SO ₂	Krotkov <i>et al.</i>	2006
Scanning Imaging Absorption Spectrometer for Atmospheric Chartography	SCIAMACHY	UV	SO ₂ BRO	Afe <i>et al.</i> Afe <i>et al.</i>	2004 2004
Spinning Enhanced Visible and Infrared Imager	SEVIRI	TIR	SO ₂ Ash	— —	— —
Total Ozone Mapping Spectrometer	TOMS	UV	SO ₂	Carn <i>et al.</i>	2003
TIROS Operational Vertical Sounder	TOVS	TIR	SO ₂	Prata <i>et al.</i>	2003

2.6 THE VOLCANOLOGICAL CONTEXT

2.6.1 Overview of following chapters

In the following chapters of this book, the fundamental, underpinning physics from this chapter is applied in more detail to several specific volcanological needs, including observations of (i) volcanic

emissions to the atmosphere, (ii) temperature changes in lava domes, (iii) hazardous flows, (iv) edifice deformation, (v) spectral characteristics of surface material, and (vi) morphology and form. It should be noted that not one of the sensors used in these studies was specifically designed to observe volcanic processes.

2.6.2 Past and current missions

Data from several geostationary and low Earth orbit satellites are currently being used to study volcanic processes. Table 2.3 provides a limited summary of the popular past and current satellites and sensors used in volcano remote sensing, with examples for each sourced mainly from the study of volcanic emissions.

2.6.3 Future missions

As stated in Section 2.6.1 there has never been a dedicated satellite mission to observe volcanoes. Volcanoes are part of the lithosphere–atmosphere exchange system and are clearly important targets in terms of satellite missions primarily designed to observe something else. The fact that they make such good targets, somewhat paradoxically, means that it is unlikely to have a dedicated satellite mission to observe volcanoes. They can be (and are) observed, quantified, and monitored by numerous sensors at a range of spatial, temporal, and spectral resolutions, and it is possible to see volcanic signatures in almost all types of remote-sensing data. So, instead of discussions about future missions targeting volcanoes, we instead must talk about sensors which have the ability to observe volcanoes and their products. Rather than detail them in a table, which immediately dates a manuscript (launch dates, mission lifetimes, and mission objectives are incredibly changeable) we respectfully point the reader towards the most complete description of the forthcoming EOS missions: <http://science.hq.nasa.gov/missions/phase.html>

2.7 SUMMARY

Satellite remote sensing is now recognized and used as a valuable tool for observing and monitoring volcanoes. This is especially true when the volcano of interest is politically inaccessible, or geographically remote, or likely to erupt in the near future and viewed as a potential hazard.

Remotely sensed data, by definition, are potential solutions to inverse problems. They are inherently abstract and require careful consideration and manipulation to determine the specifics about the object or phenomenon of interest. When applied to volcanism, remotely sensed data can yield primary information about the temperature, emissivity, deformation, emitted products (both ground-based

and atmospheric), characteristics, and the lateral extent of deposits. These data can be used to determine risk, activity level, extent of impact, and potential changes in eruptive style. Ground-based monitoring is typically of higher resolutions, but has several drawbacks including a necessity for proximity to the system and an inability to qualify the system as a whole. Only from the synoptic perspective of satellite-based instrumentation can large-scale volcanic systems be studied as a whole. The volcanoes of the North Pacific are a perfect example of this. Some are so remote and inaccessible that they are currently only monitored from space.

2.8 REFERENCES

- Afe, O.T.; Richter, A.; Sierk, S.; Wittrock, F.; Burrows, J.P. (2004). BrO Emission from volcanoes: A survey using GOME and SCIAMACHY measurements, *Geophys. Res. Lett.*, **31**, L24113, doi: 10.1029/2004GL020994.
- Bohren, C.F.; Huffman, D. (1983). *Light Scattering and Absorption by Small Particles*, Wiley, New York.
- Carn, S.A.; Krueger, A.J.; Bluth, G.J.S.; Schaefer, S.J.; Krotkov, N.A.; Watson, I.M.; Datta, S. (2003). Volcanic eruption detection by the Total Ozone Mapping Spectrometer (TOMS) instruments: A 22-year record of sulfur dioxide and ash emissions., in C. Oppenheimer, D.M. Pyle, and J. Barclay (Eds.), *Volcanic Degassing*, Special Publication 213, Geological Society, London, pp. 177–202.
- Carn, S.A.; Strow, L.L.; de Souza-Machado, S.; Edmonds, Y.; Hannon, S. (2005). Quantifying tropospheric volcanic emissions with AIRS: The 2002 eruption of Mt. Etna (Italy), *Geophys. Res. Lett.*, **32**(2), L02301, doi: 10.1029/2004GL021034.
- Dean, K.G.; Dehn, J.; Papp, K.R.; Smith, S.; Izbekov, P.; Peterson, R.; Kearney, C.; Steffke, A. (2004). Integrated satellite observations of the 2001 eruption of Mt. Cleveland, *Alaska Journal of Volcanology and Geothermal Research*, **135**(1–2), July 15, 51–73.
- Ellrod, G.; Schreiner, A. (2004). Volcanic ash detection and cloud top height estimates from the GOES-12 Imager: Coping without a 12 μ m infrared band. *Geophys. Res. Lett.*, **31**, L15110.
- Gu, Y.; Rose, W.I.; Schneider, D.J.; Bluth G.J.S.; Watson, I.M. (2005). Advantageous GOES IR results for ash mapping at high latitudes: Cleveland eruptions 2001, *Geophys. Res. Lett.*, **32**, L02305.
- Guo, S.; Rose, W.I.; Bluth G.J.S.; Watson, I.M. (2004). Particles in the great Pinatubo volcanic cloud of June 1991: The role of ice, *Geochemistry, Geophysics*,

- Geosystems*, **5**(5), Q05003, doi: 10.1029/2003GC000655.
- Harris, A.J.L.; Pilger, E.; Flynn, L.P.; Garbeil, H.; Mougini-Mark, P.J.; Kauahikaua, J.; Thornber, C. (2001). Automated, high temporal resolution, thermal analysis of Kīlauea volcano, Hawaii, using GOES-9 satellite data, *Int. J. Remote Sensing*, **22**(6), 945–967.
- Henney, L.A. (2012). Remote sensing of volcanic plumes using the advanced spaceborne thermal emission and reflection radiometer. PhD dissertation, Michigan Technical University, Houghton, MI, 297 pp.
- Khokhar, M.F.; Frankenberg, C.; Beirle, S.; Kühl, S.; Van Roozendaal, M.; Richter, A.; Platt U.; Wagner, T. (2005). Satellite observations of atmospheric SO₂ from volcanic eruptions during the time period of 1996 to 2002, *Journal of Advances in Space Research*, **36**(5), 879–887, doi: 10.1016/j.asr.2005.04.114, 2005
- Krotkov, N.A.; Carn, S.A.; Krueger, A.J.; Bhartia, P.K.; Yang, K. (2005). Band residual difference algorithm for retrieval of SO₂ from the Aura Ozone Monitoring Instrument (OMI), *IEEE Trans. Geosci. Remote Sensing* (in press).
- Mougini-Mark, P.J.; Crisp, J.A.; Fink, J.H. (2000). *Remote Sensing of Active Volcanism*, Geophysical Monograph 116, American Geophysical Union, Washington, D.C.
- Oppenheimer C. (1991). Lava flow cooling estimated from Landsat Thematic Mapper infrared data: The Lonquimay eruption (Chile, 1989), *J. Geophys. Res.—Solid Earth*, **96**, 21865–21878.
- Patrick M.R.; Smellie, J.L.; Harris, A.J.L.; Wright, R.; Dean, K.; Izbekov, P.; Garbeil, H.; Pilger, E. (2005). First recorded eruption of Mount Belinda volcano (Montagu Island), South Sandwich Islands, *Bull. Volcanol.*, **67**(5), June, 415–422, available at <http://dx.doi.org/10.1007/s00445-004-0382-6>
- Prata, A.J.; Rose, W.I.; Self, S.; O'Brien, D. (2003). Global, long-term sulphur dioxide measurements from TOVS data: A new tool for studying explosive volcanism and climate, in A. Robock and C. Oppenheimer (Eds.), *Volcanism and the Earth's Atmosphere*, pp. 75–92, Geophysical Monograph 139, American Geophysical Union, Washington, D.C.
- Read, W.G.; Froidevaux, L.; Waters, J.W. (1993). Microwave Limb Sounder measurement of stratospheric SO₂ from the Mt. Pinatubo volcano, *Geophys. Res. Lett.*, **20**, 1299–1302.
- Rees, W.G. (2001). *Physical Principles of Remote Sensing*, Cambridge University Press, Cambridge, U.K.
- Rose, W.I.; Bluth G.J.S.; Ernst, G.G.J. (2000). Integrating retrievals of volcanic cloud characteristics from satellite remote sensors: A summary, *Philosophical Transactions of Royal Society, Series A*, **358**(1770), 1585–1606.
- Watson, I.M.; Realmuto, V.J.; Rose, W.I.; Prata, A.J.; Bluth, G.J.S.; Gu, Y.; Bader, T.Yu (2004). Thermal infrared remote sensing of volcanic emissions using the moderate resolution imaging spectroradiometer, *J. Volcanol. Geothermal Res.*, **135**, 75–89.
- Wen, S.; Rose, W.I. (1994). Retrieval of sizes and total masses of particles in volcanic clouds using AVHRR bands 4 and 5, *J. Geophys. Res.*, **99**(D3), 5421–5431.
- Wright, R.; Carn, S.A.; Flynn, L.P. (2005). A satellite chronology of the May–June 2003 eruption of Anatahan volcano, *J. Volcanol. Geothermal Res.*, **146**, 102–116.

Monitoring Volcanoes in the North Pacific
Observations from Space

Dean, K.G.; Dehn, J.

2015, XXXIII, 363 p. 225 illus., 33 illus. in color. With
online files/update., Hardcover

ISBN: 978-3-540-24125-6